DOI 10.1007/s11182-024-03260-8

Russian Physics Journal, Vol. 67, No. 9, September, 2024

MICROSTRUCTURE AND PHASE COMPOSITION OF 3D PRINTED TITANIUM METAL MATRIX COMPOSITES BASED ON Ti-Al-V-Fe SYSTEM AND REINFORCED WITH TiC PARTICLES

A. V. Panin,[1,2] M. S. Kazachenok,[1] T. A. Lobova,[1] G. A. Pribytkov,[1] A. A. Panina,[2] and S. A. Martynov[1]

UDC 621.791

The ability to fabricate Ti–3Al–4V–9Fe/TiC *metal matrix composites using the wire-feed electron beam additive technology is demonstrated.* Ti–6Al–4V *titanium alloy rods surface saturated with carbon are used as the feedstock. The microstructure and phase composition of the* Ti–6Al–4V *rods subjected to carburization and as-built* Ti–3Al–4V–9Fe/TiC *composites are studied using optical and scanning electron microscopy, as well as X-ray diffraction analysis. The concentration of alloying elements in the feedstock and the composite is measured by the energy-dispersive analysis. Different patterns of* TiC *particle distribution within β grains of 3D printed* Ti–3Al–4V–9Fe/TiC *composite and along their boundaries are demonstrated. It is shown that the formation of equiaxed β grains and carbide* (TiC) *and intermetallic* (TiFe) *phases results in a high microhardness of the 3D printed* Ti–3Al–4V–9Fe/TiC *composite of 7 GPa.*

Keywords: metal matrix composites, wire-feed electron beam additive manufacturing, titanium alloys, microstructure, phase composition, Ti–Al–V–Fe/TiC.

INTRODUCTION

In recent decades, metal matrix composites (MMCs) based on titanium and its alloys reinforced with high-strength ceramic particles, such as TiC, TiB and SiC, have attracted an increasing attention due to their highly promising use as components and structural elements operating under high mechanical and thermal loads [1]. It is the combination of hard and stiff ceramic particles and ductile titanium matrix which provides high mechanical and tribological properties of these composites, even at elevated temperatures. Titanium carbide and boride (TiC and TiB) and their mixtures are among the most preferred materials for titanium matrix reinforcement due to their excellent thermodynamic and chemical stability, high hardness, and low coefficient of thermal expansion [2, 3].

The disadvantages of traditional methods of producing metal matrix composites, such as casting and powder metallurgy, include their complexity and high production cost. There is currently a significant interest in the fabrication of metal matrix composites using additive technologies. This allows the creation of volumetric products with complex shapes by applying the material layer by layer according to a three-dimensional computer model. The most common additive manufacturing method for titanium metal matrix composites is the laser melting of titanium or titanium alloy powders with other ceramic powders, such as TiC, TiB, etc. This process has been described in sufficient detail [4–6].

A more promising approach is the method of simultaneous laser or electron beam melting of ceramic powders and titanium wire [7–9]. Alternatively, electron beam melting of the titanium wire alloyed with carbon, boron, silicon, and other carbide-forming elements [10, 11], may also prove effective. The advantage of this method is a higher rate of

[1]Institute of Strength Physics and Materials Science of the Siberian Branch of the Russian Academy of Sciences, Tomsk, Russia, e-mail: pav@ispms.ru; kms@ispms.ru; tal@ispms.ru; gapribyt@mail.ru; martynov@ispms.ru; [2]National Research Tomsk Polytechnic University, Tomsk, Russia, e-mail: sonaa@tpu.ru.
Original article submitted July 19, 2024, accepted for publication August 28, 2024.

layer-by-layer growth, which significantly reduces the cost of the 3D printing process of metal matrix composites. Furthermore, the temperatures and size of the molten pool produced by electron-beam melting of wire feedstock appear to be quite high and large, respectively, which enables more effective implementation of ex-situ and in-situ techniques for manufacturing metal matrix composites.

An additional way to improve the strength of Ti–6Al–4V-based titanium metal matrix composites is to replace vanadium, which is a β-isomorphic stabilizer, with cheaper iron, which is a β-eutectoid stabilizing element. It is well-known that the β phase is decomposed into α′, α″ and ω phases upon quenching of titanium alloys containing β-isomorphic stabilizers. Iron lowers the polymorphic transformation temperature to the eutectoid decomposition temperature. As a result, the decomposition of the iron solid solution in titanium leads to the formation of α phase and Fe-based intermetallic compounds. In addition, the introduction of iron can lead to solutal undercooling and thus inhibit the columnar grain growth [12]. In turn, the presence of aluminum in the Ti-Al-Fe alloy system prevents the formation of iron oxides at interfacial boundaries, thereby increasing its oxidation resistance [13].

The aim of this work is to study the possibility of fabricating titanium metal matrix composites based on Ti–Al–V–Fe system hardened with TiC particles by electron beam additive manufacturing. This research investigates the microstructural characteristics and microhardness of the composites.

1. MATERIALS AND METHODS

To fabricate a 3D-printed titanium metal matrix composite we used thin square rods 150 mm long and 1.5 mm^2 in cross-sectional area, which were cut from a wrought Ti–6Al–4V titanium alloy plate with the following chemical composition (wt.%): 6.6 Al, 4.0 V, 0.2 Fe, 0.01 C, 2.6 O, 0.05 N and balance titanium. The cut rods subjected to acid etching (HF solution), cleaning with alcohol followed by carbonization served as a feedstock material for 3D printing. Carbonization (i.e. the process of diffusion saturation with carbon) consisted in placing the Ti–6Al–4V rods in a heat-resistant container filled with carbon black P-803, covering the rods with carbon black on all sides, then heating them in vacuum to a temperature of 1200°C, holding for 4 hours, followed by gradual cooling. After cooling, the rods were removed from the backfill and the adhering soot was carefully removed from the surface with a dry cloth, and the rods were weighed. The increase in the weight of the Ti–6Al–4V rods (weight gain) as a result of diffusion saturation was 0.8 wt.%.

In the additive manufacturing process, individual Ti–6Al–4V rods subjected to preliminary carbonization were placed in a feeder pusher and fed through the feeder into the print area. This process is described in more detail elsewhere [14]. At the same time, an electron beam was used to vaporize a nearby iron plate. This technology allows us to add various alloying elements (in this case, Fe) to the composite by controlling the electron beam power.

The laboratory electron beam additive manufacturing setup, developed at ISPMS SB RAS (Tomsk, Russia), was equipped with a thermal field-emission electron gun. The electron beam additive manufacturing process was carried out at a residual pressure in the chamber of up to 5×10^{-5} Pa and a beam acceleration voltage of 30 kV. The distance between the electron beam source and the baseplate with the dimensions of 150 mm × 150 mm × 10 mm was 630 mm. The feed rate was 2 m/min. The first three layers were formed at a beam current of 24 mA followed by its decreasing to 21 mA. The hatch spacing between the adjacent tracks within the same layer was ~ 3 mm. After welding each layer of the baseplate moved down by 3 mm. 3D-printed billets were separated from the baseplate and cut along the growth direction into 2 mm-thick plates using spark cutting.

An Axiovert 40 MAT optical microscope and an Apreo 2S scanning electron microscope (SEM) equipped with a Pegasus integrated energy dispersive X-ray spectrometry (EDS) and electron backscatter diffraction (EBSD) systems were employed for the microstructural characterization of the Ti–6Al–4V rods and as-built Ti–3Al–4V–9Fe/TiC composites using both plan view and cross section geometries. For the metallographic and EBSD analysis, the samples were subjected to mechanical grinding and polishing followed by etching with Kroll's reagent. The EBSD characterization was performed with a tungsten cathode at an accelerating voltage of 20 kV. The data acquisition was performed with a step size of 0.02–0.50 μm.

An X-ray diffraction (XRD) analysis of the Ti–6Al–4V rods and as-built Ti–3Al–4V–9Fe/TiC composites was carried out using a Shimadzu XRD-7000 diffractometer with Cu Kα-radiation (λ = 0.15406 nm) according to the

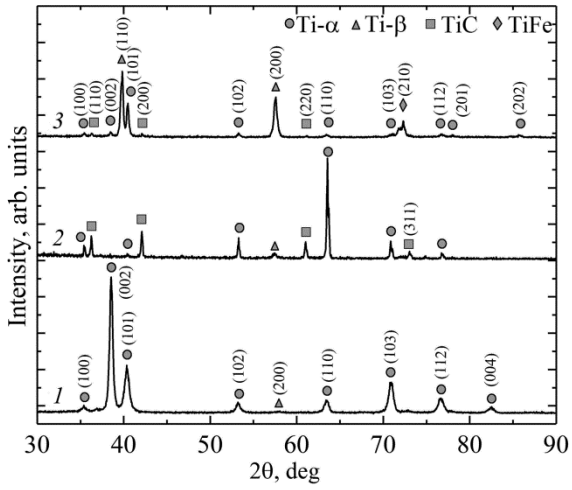

Fig. 1. Selected sections of diffraction patterns from Ti–6Al–4V rods before (*1*) and after carbonization (*2*) and from as-built Ti–3Al–4V–9Fe//TiC composite (*3*).

conventional symmetric Bragg-Brentano geometry [15] at room temperature. The XRD studies were performed in the θ–2θ scanning mode from 30° to 90° angular range with a scan speed of 1.2°/min.

Microhardness of the as-built Ti–3Al–4V–9Fe/TiC composite was measured using a PMT-3 hardness tester with a load on the diamond pyramid of 50 g.

2. RESULTS AND DISCUSSION

A comparison of the X-ray diffractograms of the Ti–6Al–4V rods before and after diffusion saturation with carbon, demonstrates the effectiveness of this method for forming the feedstock containing carbide phase. According to diffractogram 1 (Fig. 1), the diffraction peaks corresponding to different crystallographic planes of α-Ti are only present in the XRD pattern of the uncarbonized Ti–6Al–4V rod. The presence of β-Ti phase evidences of the XRD peak broadening at 2θ = 40.2°, belonging to α-Ti (101). This particular peak shape can be considered as the superposition of several peaks for α-Ti (101) and β-Ti (110). The structure of the surface layers of the titanium rods changes significantly after carburization. First, the preferred orientation of the α phase is shown in Fig. 1, diffractogram 2. Moreover, there is a pronounced XRD peak corresponding to the β phase (200). However, the volume fraction of β phase does not exceed 1%. The latter is due to the presence of carbon, which is an α stabilizing element in titanium. There is also the formation of titanium carbide TiC whose volume fraction in the surface layer of carbonized Ti–6Al–4V rod reaches 28%.

Metallographic studies of the cross-section of Ti–6Al–4V rods confirm significant changes in their microstructure during the carbonization process (Fig. 2*b*). First, there is an intensive growth of primary β grains from 2 μm to 2 mm. In addition, due to the high cooling rate a large amount of massive martensite is formed and the transverse dimensions of the lamellae of α/α′ phase reach 20 μm.

Taken together, the EDS data and SEM micrographs of the surface of carbonized Ti–6Al–4V rods reveal the presence of a carbonaceous coating of an inhomogeneous thickness (Fig. 2*a*). A homogeneous coating is formed in the areas of the dense contact of the rods with the carbon black (Fig. 2*a*, Table 1). Its thickness reaches 15 μm (Fig. 2*c*). Conversely, there is no carbon in the areas of the Ti–6Al–4V rods in close contact with each other during carburization. It is seen in Fig. 2*c* and Table 2 that the maximum carbon concentration (28 wt.%) is observed near the coating surface, and it gradually decreases at the approach to the titanium substrate. In addition, oxygen is detected in the uppermost surface layer of the coating, reaching 11 wt.%. It should be noted that the large variation in the amount of vanadium in

TABLE 1. Elemental Composition of Carbonized Ti–6Al–4V Rod in Points Shown in Fig. 2*a*

Location / Element	Point 1, wt.%	Point 2, wt.%	Point 3, wt.%	Point 4, wt.%	Point 5, wt.%	Point 6, wt.%	Point 7, wt.%	Point 8, wt.%
Al	–	–	–	–	–	7	10	9
V	–	–	–	–	–	11	3	1
Ti	72	72	67	79	58	81	87	90
C	28	28	33	21	42	–	–	–

TABLE 2. Elemental Composition of Carbonized Ti–6Al–4V Rod in Points Shown in Fig. 2*c*

Location / Element	Point 1, wt.%	Point 2, wt.%	Point 3, wt.%	Point 4, wt.%	Point 5, wt.%	Point 6, wt.%	Point 7, wt.%
Al	–	–	–	5	5	7	6
V	–	–	–	15	10	4	3
Ti	66	88	91	80	85	89	93
C	23	12	9	–	–	–	–
O	11	–	–	–	–	–	–

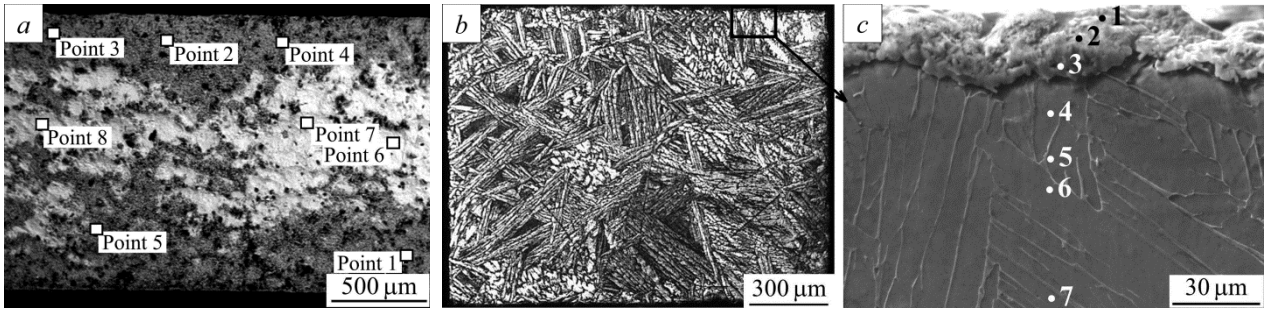

Fig. 2. SEM (*a*, *c*) and optical (*b*) images of surface (*a*) and cross-section (*b*, *c*) of carbonized Ti–6Al–4V rod. Solid black line box in (*b*) highlights area enlarged in (*c*).

the bulk of the Ti–6Al–4V rod is due to its different contents in the lamellae of α/α′ phase and in the layers of residual β phase.

A Ti–3Al–4V–9Fe/TiC titanium metal matrix composite is formed by electron beam melting of the carbonized Ti–6Al–4V rods with a simultaneous introduction of Fe into the molten pool. As shown in Fig. 3, the microstructure of the 3D printed Ti–3Al–4V–9Fe/TiC composite consists of columnar and equiaxed β grains. The average transverse size of columnar β grains is 100 μm. The size of equiaxed β grains varies from 20 to 50 μm. It is worth noting that the lamellae of α/α′ phase are occasionally observed in individual β grains (Fig. 3*c*). The latter is due to the heterogeneous distribution of Fe, which is an α-stabilizer element in titanium. According to the EDS data, the Fe content in β grains reaches 10 wt.%, which is explained by the large (up to 22 at.%) equilibrium solubility of iron in β phase. In turn, the amount of Fe in the grains containing lamellae of α/α′ phase varies in the range of 2–4%. It can be assumed that during the molten pool cooling a polymorphic β→α transformation takes place within the primary β grains, which are characterized by a lower Fe content, leading to the formation of the α/α′ phase.

An EBSD analysis shows TiC particles both inside β grains and along their boundaries in the 3D printed Ti–3Al–4V–9Fe/TiC composites (Fig. 3*c, d*). The TiFe precipitates with curved shapes are homogeneously distributed within β grains (Fig. 4), while TiC particle agglomerates with the sizes of up to 5 μm are observed inside α grains

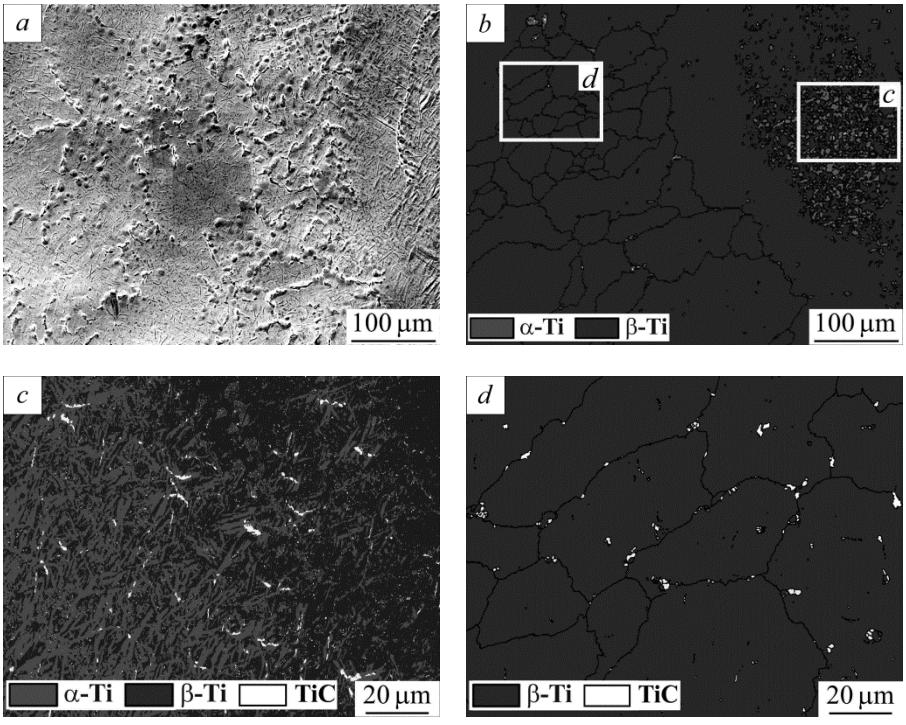

Fig. 3. SEM image (*a*) and EBSD phase identification maps (*b*-*d*) of as-built Ti–3Al–4V–9Fe/TiC composite. Solid white line boxes in (*b*) highlight areas enlarged in (*c*, *d*).

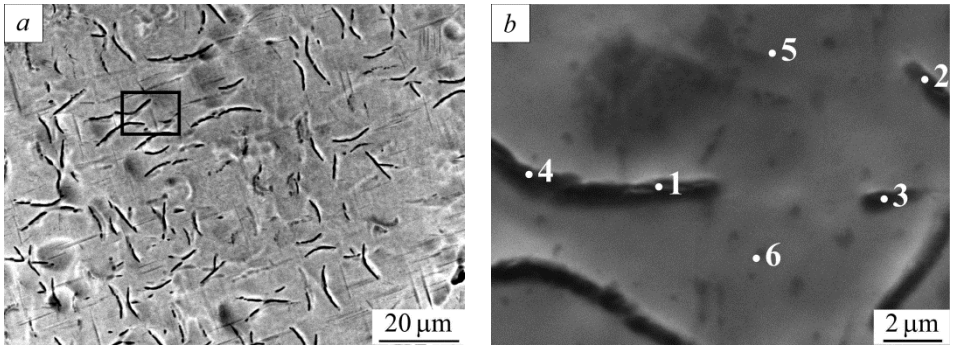

Fig. 4. SEM images from as-built Ti–3Al–4V–9Fe/TiC composite. Solid black line box in (*a*) highlights area enlarged in (*b*).

(Fig. 3*c*) and at the boundaries of β grains (Fig. 3*d*). It is worth noting that the grain boundary segregation of the carbides can embrittle the composite material and is therefore not desirable.

The elemental composition of β grains in the 3D printed Ti–3Al–4V–9Fe/TiC composite is presented in Table 3. The carbon content in the carbide particles is approximately 5% wt., while no carbon is found in the titanium matrix, as shown in Table 3. The latter is due to the fact that the maximum solubility of carbon in the α phase does not exceed 0.4 at.% at 500°C and increases only to ~1.5 at.% at 900°C [16]. In turn, the maximum solubility of carbon in the β phase does not exceed 0.6 at.% in the temperature range of 920–1300°C.

The phase composition of the 3D printed Ti–3Al–4V–9Fe/TiC composite was clearly demonstrated by the XRD analysis. The XRD pattern of the composite shows the peaks corresponding to different crystallographic planes of the α-phase and distinct diffraction peaks corresponding to β-Ti (110) and β-Ti (200) (see Fig. 1, diffractogram 3). The

TABLE 3. Elemental Composition of As-built Ti–3Al–4V–9Fe/TiC Composite in Points shown in Fig. 4*b*

Location / Element	Point 1, wt.%	Point 2, wt.%	Point 3, wt.%	Point 4, wt.%	Point 5, wt.%	Point 6, wt.%
Al	3	2	3	3	3	4
V	5	3	4	4	5	5
Ti	79	81	81	81	82	82
C	4	6	4	3	–	–
Fe	9	8	8	9	10	9

volume fraction of β phase is 57%. The high (8–10 wt.%) Fe content is responsible for such a high residual β-phase content. Furthermore, there is a peak at 72.2°, which is attributed to the (210) plane of the TiFe phase. The volume fraction of the TiFe phase reaches 8%. It can be assumed that this phase is formed as a result of the eutectoid decomposition of β-Ti → α-Ti + TiFe occurring at a temperature of 590°C during the molten pool cooling in local areas with low Fe content. Again, the peaks at the angles 2θ = 36.3, 42.1 and 61.1° are evidence for the presence of TiC phase. The volume fraction of the TiC phase is about 3%.

The 3D printed Ti–3Al–4V–9Fe/TiC composite has a high microhardness of 7 GPa due to the presence of the carbide and intermetallic phases. Meanwhile, the microhardness of the as-built Ti–6Al–4V sample manufactured under similar 3D printing parameters is 4.1 GPa only [17].

CONCLUSIONS

The possibility of producing titanium metal matrix composite based on the Ti–Al–V–Fe system reinforced with TiC particles by the electron beam additive technology has been demonstrated. Thin square rods 150 mm long and 1.5 mm^2 in cross-sectional area, cut from a wrought Ti–6Al–4V titanium alloy plate followed by diffusion saturation with carbon, served as a feedstock material for 3D printing. This method of feedstock preparation makes it possible to control the amount of the carbide phase in the titanium metal matrix composite and to achieve a homogeneous distribution of the carbide particles in the 3D printed sample. An addition of iron to the molten pool during the additive manufacturing process has been shown to suppress columnar grain growth in the titanium metal matrix composite. Moreover, its presence leads to the formation of intermetallic phases. This provides an additional contribution to the hardening of 3D printed titanium metal matrix composites.

It has been shown that it is possible to fabricate a 3D printed composite based on the Ti–Al–V–Fe system containing 3 wt.% TiC by using a feedstock of the titanium alloy Ti–6Al–4V rods exposed to carbon black at a temperature of 1200°C for 4 hours. Spherical TiC particles with an average size of 0.5 μm are arranged both inside β grains and along their boundaries in the 3D printed Ti–3Al–4V–9Fe/TiC composite. Spherical TiC particles with an average size of 0.5 μm form agglomerates of carbide particles with a size of up to 5 μm both inside α grains and along β grain boundaries in the 3D printed Ti–3Al–4V–9Fe/TiC composite. TiFe precipitates with curved shape are homogeneously distributed within the β grains.

The formation of the equiaxed β grains with a size of 20 – 50 microns and the carbide (3 wt.%) and intermetallic (8 wt.%) phases results in a high microhardness of the 3D printed Ti–3Al–4V–9Fe/TiC composite, equal to 7 GPa.

COMPLIANCE WITH ETHICAL STANDARDS

Author contributions

A.V.P.: conceptualization, writing – original draft preparation, review and editing; K.M.S.: investigation, writing – original draft preparation; T.A.L.: analysis and visualization; G.A.P. methodology, writing – review and editing; A.A.P.: investigation; S.A.M.: investigation. All authors discussed the results and contributed to the final manuscript. All authors have read and agreed to the published version of the manuscript.

Conflicts of interest

The authors declare that they have no known competing financial interests or personal relationships that could have appeared to influence the work reported in this paper.

Funding

The study was financially supported by the Russian Science Foundation (Project No. 24-19-00604), The investigations have been carried out using the equipment of Share Use Centre "Nanotech" of the ISPMS SB RAS and the CSU NMNT TPU.

Financial interests

The authors have no relevant financial or non-financial interests to disclose.

Institutional review board statement

Applicable.

REFERENCES

1. M. D. Hayat, H. Singh, Z. He, and P. Cao, Compos. A: Appl. Sci. Manuf., **121**, 418 (2019). http://10.1016/j.compositesa.2019.04.005.
2. O. E. Falodun, B. A. Obadele, S. R. Oke, and A. M. Okoro, Int. J. Adv. Manuf. Tech., **102**, 1689 (2019). http://10.1007/s00170-018-03281-x.
3. M. Yi, X. Zhang, G. Liu, *et al*., Mater. Charact., **140**, 281 (2018). http://doi.org/10.1016/j.matchar.
4. Y. Yang, J. Zhang, and W. Wei, Mater. Sci. Eng., A., **829**, 144829 (2023). http://doi.org/10.1016/j.msea.2023.144829.
5. C. Yu, X. Liu, Y. Li, *et al*., nt. J. Mech. Sci., **205**, 106595 (2021). http://doi.org/10.1016/j.ijmecsci.2021.106595.
6. J. Wang, L. Tang, Y. Xue, *et al*., J. Mater. Res. Technol., **28**, 3110 (2024). http://doi.org/10.1016/j.jmrt.2023.12.227.
7. P. K. Farayibi, Adv. Eng. For., **26**, 22 (2018). http://doi.org/10.4028/www.scientific.net/AEF.26.22.
8. Z. Hua, L. Xiong, M. Zhang, et al., Compos. B Eng., 263, 110817 (2023); http://doi.org/10.1016/j.compositesb.2023.110817.
9. A. V. Panin, M. S. Kazachenok, E. A. Sinyakova, *et al*., Mat. Des. Proc. Com., **3**, 136 (2021). http://doi.org/10.1002/mdp2.136.

10. H. Wang, Z. Yao, Tao X., *et al*., Vacuum, **172**, 109053 (2020). https://doi.org/10.1016/j.vacuum.2019.109053.
11. Z. Chen, Y. Peng, X. Zhang, *et al*., J. Mater. Res. Tech., **23**, 1347 (2023). https://doi.org/10.1016/j.jmrt.2023.01.065.
12. M. Chen, S. V. Petegem, Z. Zou, *et al*., Addit. Manuf., **59**, 103173 (2022). https://doi.org/10.1016/j.addma.2022.103173.
13. E. Reverte, S. A. Tsipas, and E. Gordo, Metals, **10**, 254 (2020). https://doi.org/10.3390/met10020254.
14. K. Osipovich, K. Kalashnikov, A. Chumaevskii, *et al*., Metals, **13**, 279 (2023). https://doi.org/10.3390/met13020279.
15. T. Ida and H. Toraya, J. Appl. Cryst., **35**, 58 (2002). http://doi.org/10.1107/S0021889801018945.
16. V. Trush and A. Luk'yanenko, Uk. J. Mech. Eng. Mater. Sci., **4**, 29 (2018). https://doi.org/10.23939/ujmems2018.01.029.
17. A. V. Panin, M. S. Kazachenok, K. V. Krukovsky, *et al*., Phys. Mesomech., **26**, 643 (2023). http://doi.org/10.1134/S1029959923060048.